ISIJ International, Vol. 58 (2018), No. 7, pp. 1332–1340

Fractographical Analyses of Crack Initiation Site in High-cycle Fatigue for Ti–Fe–O Alloy at Low Temperature

Osamu UMEZAWA,[1)]* Takayuki YUASA[2)] and Weibo LI[3)]

1) Faculty of Engineering, Yokohama National University, 79-5 Tokiwadai, Hodogaya, Yokohama, 240-8501 Japan.
2) Graduate School of Engineering, Yokohama National University. Now at Nippon Steel & Sumitomo Metal Corp, 3 Hikari, Kashima, 314-0014 Japan.
3) Graduate School of Engineering, Yokohama National University, 79-5 Tokiwadai, Hodogaya, Yokohama, 240-8501 Japan.

(*Received on November 14, 2017; accepted on March 27, 2018*)

High-cycle fatigue properties of a Ti–Fe–O alloy with different processed products such as rolled plate (L and T), cross-rolled plate (CR) and groove-rolled bar (CS) were evaluated at 77 K and 293 K. Fine equiaxed α grains randomly oriented with [0001] perpendicular to tensile axis were produced in the CS. No significant difference of 10^7 cycles fatigue strength was recognized among the test materials at each temperature, although the CS exhibited an improved fatigue strength in long-life regime at 293 K. The subsurface crack initiation was dominant in lower stress level and at 77 K. The subsurface crack initiation sites consisted of facet or facets. The facets were identified as (0001) in the L, T and CR. In the CS, the (0001) facet provided an origin of subsurface crack initiation site, but the $\{10\bar{1}0\}$ facets mainly covered the sites at 77 K. The combination of shear stress and opening stress on $\{10\bar{1}0\}$ may be responsible for forming a facet and its growth in the neighboring grain. The dependence of subsurface crack initiation site size on the maximum stress range was evaluated, where the maximum stress intensity factor range, ΔK_{Imax}, revealed the temperature and stress dependences.

KEY WORDS: texture; macrozone; transgranular crack; titanium alloys; fatigue; subsurface crack initiation; low temperature.

1. Introduction

In near α and α-β type titanium alloys, subsurface fatigue crack initiation occurs apparently without the existence of any defects such as inclusion or pore and is dominant in the high-cycle regime and at lower temperatures. Crystallographic transgranular facet or facets are commonly detected at the crack initiation site.[1,2)] Each fact is fitted to α grain morphology or microstructure, and mostly the facets formed on or near the (0001) basal plane regardless their inclination to the principal stress axis.

Dislocation movement in α phase is restricted on the primary slip plane and fairly planar under high-cycle fatigue so that dislocation arrays on $\{10\bar{1}0\}<11\bar{2}0>$ are piled-up in the vicinity of α grain boundaries and a local stress concentration generates near the boundaries.[3)] The microstructural design to refine the α-grain structure and to distribute its crystal orientation randomly may reduce the maximum of stress concentration, and then improve the high-cycle fatigue strength. In fact, the microstructural modification in Ti-6Al-4V alloys by thermomechanical treatment as equiaxed α grain structure with a few μm in diameter and fine β particles introduced much higher fatigue strength at cryogenic temperature.[4)] In the conventional hot-rolled and annealed plate, however, the microtexture consisted of recovered (soft) α grain region and recrystallized (hard) α grain region is developed in near α and α-β type titanium alloys. A near α type Ti–Fe–O alloy[5)] as well as Ti-6Al-4V alloys[6)] clearly exhibited the subsurface fatigue crack generation, where the strain incompatibility between soft (plastically deformed) and hard (elastically deformed) α grains under cyclic deformation may induce the (0001) microcrack and its growth in the recrystallized α grain.[3)] Slip deformation analysis based on full constraints model by Taylor theory was suggested that internal stress in α grain was developed on the normal to (0001) and hardly relaxed.[7)] The accumulated tensile stress along [0001] may be responsible for initial microcracking and its opening in the hard grain. Not only the microstructure and α grain size but also texture or macrozone (microtexture), therefore, strongly affect the subsurface fatigue crack initiation.[1)]

Bantounas *et al.*[8)] examined fatigue crack initiation of three different Ti-6Al-4V products such as unidirectionally rolled plate, cross-rolled plate and forged bar. Although the majority of facets were near-basal plane with misorientations between 15 and 40 from the loading direction, macro-zones oriented with their main c-axis texture component close to the loading direction were responsible for faceted fracture morphologies and within such macro-zones faceted crack growth was believed to occur with little resistance. Furthermore, $\{10\bar{1}0\}$ facet was reported under dwell fatigue test

* Corresponding author: E-mail: umezawa@ynu.ac.jp
DOI: http://dx.doi.org/10.2355/isijinternational.ISIJINT-2017-673

for highly textured alloy with [0001] perpendicular to tensile axis.[9] Since the simple shear mode on $\{10\bar{1}0\}$ can assist the growth of microcrack on the plane, and induce localized slip of $\{10\bar{1}0\}<11\bar{2}0>$ or $(0001)<11\bar{2}0>$,[10] the stress redistribution may play an important role in subsurface crack generation especially under dwell fatigue.[11] However, influence of α grain texture on microcrack initiation and microcrack growth to form a subsurface crack has not been clear yet. In the present study, high-cycle fatigue properties of a Ti–Fe–O alloy with different processed products such as rolled plate, cross-rolled plate and groove-rolled bar were examined at 77 K and 293 K. The processes were applied to install macrozone as the previous study[5] or texture with [0001] perpendicular to tensile axis into the alloy. Fractographical analyses on the fatigue crack initiation sites were carried out to discuss transgranular facets formation.

2. Experimental Procedure

2.1. Materials

Four kinds of thermomechanical treated materials of a near α-type Ti–Fe–O alloy were examined in an annealed condition; the main chemical compositions were as follows: 0.0005 H, 0.386 O, 0.003 N, 0.994 Fe, 0.003 C, and balance of Ti in mass%. The Ti–Fe–O alloy was double melted in vacuum arc remelting, forged (1 273 K heating), and hot rolled (1 123 K heating) to a 43-mm-thick plate. The L (longitudinal) and T (transversal) materials were taken from the 43-mm-thick plate as shown in **Fig. 1**, and their longitudinal directions were parallel to the rolling direction (RD) and the transverse direction (TD), respectively. A part of 43-mm-thick plate was cross-rolled (1 123 K heating) along the TD to a 27-mm-thick plate. The longitudinal direction of the CR (cross-rolled) material was cut parallel to the RD from the 27-mm-thick plate. The L material in a square of 43 mm was groove-rolled (1 023 K heating) to a rectangular bar in a square of 22.5 mm and cold swaged into a round bar of 20 mm in diameter. The longitudinal direction of the CS (cold-swaged) material was cut parallel to the RD from the round bar. All of the materials, *i.e.* L, T, CR and CS, were annealed at 1 023 K for 3.6 Ks, followed by air cooled.

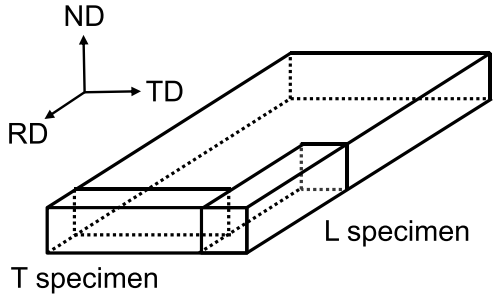

Fig. 1. Schematic illustration of the 43-mm-thick rolled plate.

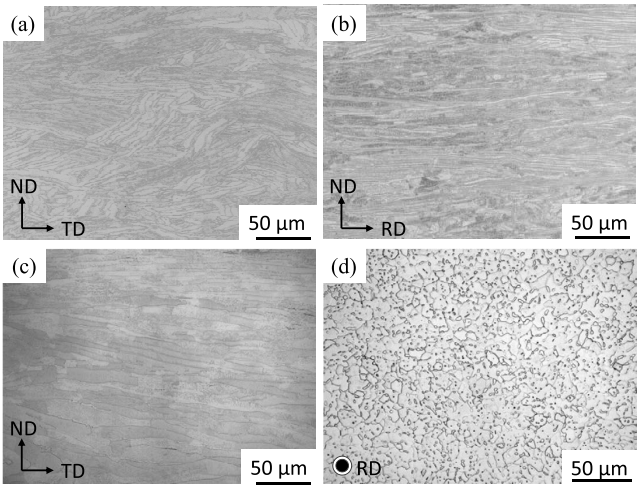

Fig. 2. Optical microstructure of (a) L, (b) T, (c) CR and (d) CS materials in the transverse section.

Optical micrographs of each material are represented in **Fig. 2**. The microstructure of L, T and CR, consisted of pancaked α grains and fine β platelets of which were aligned with each other. Each α grain elongates about 200–300 μm in length parallel to the RD as well as the TD. The microstructure of CS was equiaxed α grain structure with about 13 μm in diameter and fine β particles dispersed. Tensile tests were done at an initial strain rate of approximately 4×10^{-4} s^{-1} using a screw-driven-type tester. Cylindrical test pieces were cut parallel to the longitudinal direction of the materials; the gage geometry was 3.5 mm in diameter and 25 mm in length. The test temperatures were 77 K (immersed in liquid nitrogen) and 293 K (in ambient air). The 0.2% proof stress, $\sigma_{0.2}$, ultimate tensile strength, σ_B, and total elongation, El, were determined by duplicate tests for the test materials as shown in **Table 1**. Their strength was higher than that of the Ti–Fe–O alloy plate in the previous study[5] because of higher oxygen (a solid solution strengthen element in α phase) content.

2.2. Fatigue Testing

The configuration of hour-glass type fatigue test specimens is shown in **Fig. 3**. The specimens were machined parallel to the longitudinal direction of the materials. Fatigue testing was carried out at 77 K and 293 K. Using a servohydraulic fatigue machine, load-controlling tests were done. The sinusoidal waveform loading was uniaxial with a minimum-to-maximum stress ratio, R ($\sigma_{min}/\sigma_{max}$), of 0.01. Test frequencies of 15 Hz at 77 K and 20 Hz at 293 K were chosen so that the specimen temperature rise should be as low as possible. The fatigue tests were interrupted at the

Table 1. Tensile properties of the test materials.

Materials	$\sigma_{0.2}$ (MPa) 293 K	σ_B (MPa) 293 K	El (%) 293 K	$\sigma_{0.2}$ (MPa) 77 K	σ_B (MPa) 77 K	El (%) 77 K
L	495	770	29.7	1 169	1 299	20.1
T	550	796	21.6	1 150	1 395	3.8
CR	634	765	31.7	1 206	1 308	20.7
CS	659	799	29.5	1 257	1 326	11.3

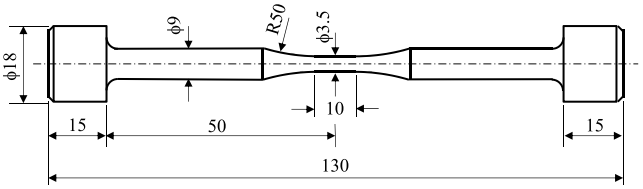

Fig. 3. Configuration of fatigue specimen in the present study.

cycles of 2×10^7.

2.3. Analyses

The mechanically polished surfaces were examined by scanning electron image (SEI) and electron backscatter diffraction (EBSD) pattern analysis in scanning electron microscopy (SEM). The sample surfaces were prepared by grinding with 1200-grit emery paper and by polishing with diamond and finally with a stirred solution of colloidal silica and H_2O_2. The etchants were Kroll's reagent (2 ml HF - 10 ml HNO_3 - 88 ml H_2O), and then a solution of 2 ml HF - 5 ml H_2O_2 - 100 ml H_2O. X-ray texture analyses on the ND (normal direction) plane were carried out using the filtered Cu-Kα radiation under 40 keV accelerating voltage with 300 mA on a texture goniometer. Schulz reflection method[12] was adopted and normalized intensity for (0001), $\{10\bar{1}0\}$ and $\{10\bar{1}1\}$ was obtained. The samples normal to the RD plane were rotated from 0 to 75 degrees, and data was recalculated to construct the full pole figures. EBSD analysis also provided the microtexture characterization. Concerning the texture representation, the $\{\phi1, \Phi, \phi2\}$ Euler angles correspond to the definition given by Bunge[13] and the crystal coordinate system is $\{X=[10\bar{1}0], Y=[\bar{1}2\bar{1}0], Z=[0001]\}$. The crystallite orientation distribution functions (ODFs) have been calculated using the harmonic method.[14]

The facets at subsurface crack initiation sites were examined by SEM. At low magnification the subsurface crack initiation sites appear flat and are inclined to the principal stress axis, and fatigue crack growth gives an appearance in a radial pattern from the initiation site.[2,6,15] According to the previous studies, the subsurface crack initiation site is defined as the whole of the inclined area (Stage I crack) which is not placed on the fatigue crack propagating plane (Stage II). The initiation site is approximated to an elliptical crack with orthographic projection on the main crack propagating plane, so that the minor axis is almost parallel to the initial crack growth direction as shown in **Fig. 4**. The size of the subsurface crack initiation site was quantified by a crack length parameter, $\sqrt{area}$,[16] which was defined as the square root of subsurface crack area for the subsurface crack initiation site on propagating plane as shown in Fig. 4.[2,6,15] 3D laser scanning microscope was also employed to characterize the facets with three-dimensional morphology and position on the fracture surface. Then EBSD analysis was applied to the crystal orientation identification of each facet.[17,18] Gonio stage in SEM was manually tilted and/or rotated to place the sample for taking EBSD pattern from the subsurface crack initiation site (facets) and to adjust each facet plane correctly facing to the EBSD camera screen.

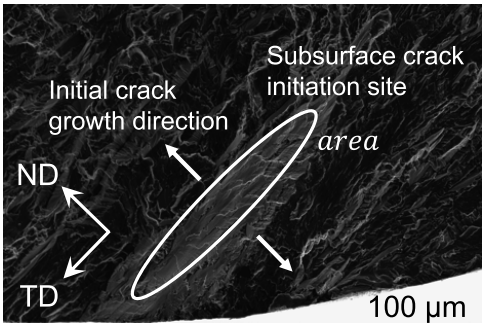

Fig. 4. Definition of $\sqrt{area}$ at subsurface fatigue crack site (CR, 293 K, σ_{max}=459 MPa, 8 714 986 cycles).

3. Results

3.1. Texture of Materials

Figure 5(a) shows X-ray texture of the 43-mm-thick rolled plate (L and T) which reveals a tendency of TD-split texture as in the cold-rolled titanium sheet.[19] There are less α grains oriented with their c axis parallel to the principal stress axis (RD). In the EBSD analysis, the microstructure of the plate is classified into two regions, which are designated as recrystallized α grains and recovered α grains as shown in Fig. 5(b). The α grain width in the recovered α grain region was about several μm, compared to about a few ten μm in the recrystallized α one. Those crystallographic texture measured by EBSD on the RD plane shown in Fig. 5(b) is drawn by (0001), $(10\bar{1}0)$ and $(11\bar{2}0)$ pole figures in Fig. 5(c). The recovered α grains showed a strong TD-split texture with $(0001)<11\bar{2}0>$ rotated counterclockwise about 25 degrees around RD where the highest pole density was over 20 as shown in Fig. 5(d), while the other α grains were dispersed around (0001)//ND plane.

The 27-mm-thick cross rolled plate (CR) shows the similar texture of the 43-mm-thick plate as shown in **Fig. 6**(a). The RD-split component is overlapped on the TD-split one. The CR provided microstructure with rather clearly divided into the two regions because of higher reduction in the rolling process,[20] where the rotation in the TD-split texture[21] and the basal texture in the recrystallized α grains were promoted. Furthermore, these rolled plates contain a macrozone (microtexture) such as recovered α grain region as the previous study.[5]

For the round bar material CS, most of α grains with their c axis were near perpendicular to the principal stress axis (RD), and near $<10\bar{1}0>$//RD fiber texture was appeared on the RD plane as shown in Fig. 6(b). The equiaxed α grains were randomly oriented with rotating (0001) along RD. Furthermore, recovered α grains were removed in the CS.

The ultimate tensile strength in T and CS was relatively higher than that in L and CR at 293 K and 77 K as shown in Table 1, and the 0.2% proof stress in the CR and CS was higher than that in the L and T. Those differences may be reflected on their texture and working ratio.

3.2. S–N Data

Figure 7(a) shows S–N data of the test materials at 77 K and 293 K with the previous data at 77 K[5] as a reference. No significant difference of 10^7 cycles fatigue strength is recognized among the test materials at each temperature, although the fatigue strength of the CS is slightly higher than that of the others at 293 K. Figure 7(b) shows the S–N data with normalizing the maximum cyclic stresses by ultimate tensile strength. The normalized 10^7 cycles fatigue strength is approximately 0.6 and superior to the previous data. The CS exhibited the highest normalized 10^7 cycles fatigue strength as 0.65 at 293 K. The normalized fatigue strength at 293 K is higher than that at 77 K in the low-cycle range as 10^4-10^5 cycles, and slightly higher even in the high-cycle range. Thus, a fine equiaxed α structure exhibited

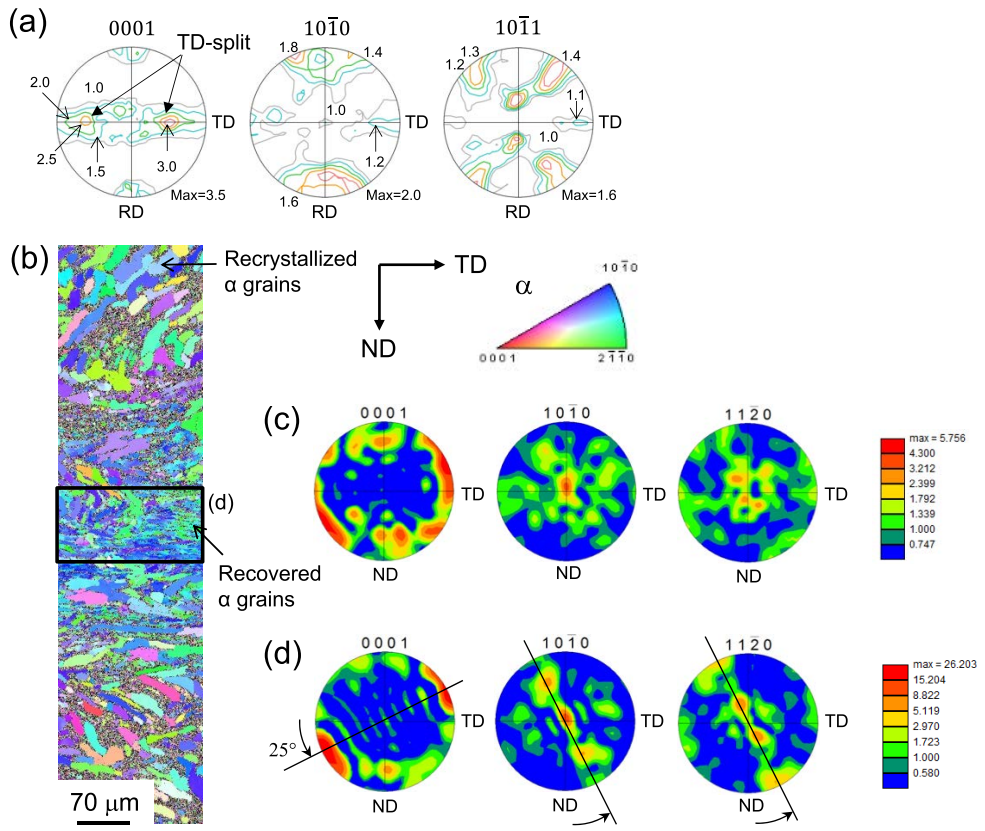

Fig. 5. Texture of the 43-mm-thick rolled plate: (a) X-ray texture on the ND plane, (b) EBSD IPF map on the RD plane, (c) α phase orientation distribution and (d) that in the recovered α grain region. (Online version in color.)

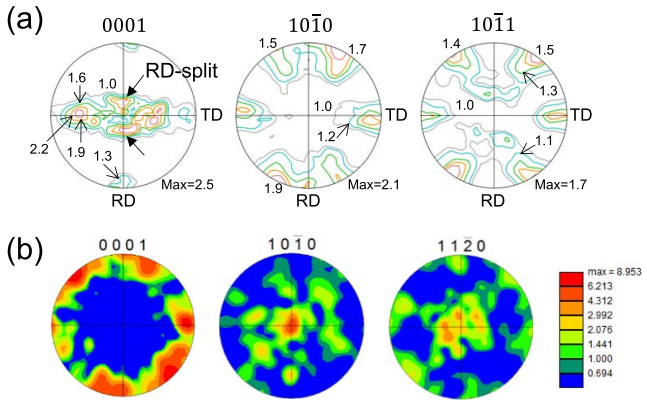

Fig. 6. X-ray texture on the ND plane of CR (a), and orientation distribution on the RD plane of CS (b). (Online version in color.)

an improved fatigue strength in long-life regime at 293 K, but not at 77 K.

3.3. Fracture Surface

Surface crack initiation indicated by open symbols appear in higher stress level at each temperature, while subsurface crack initiation indicated by solid symbols occurs in lower stress level as shown in Fig. 7(a). Especially the subsurface crack initiation is predominant mode at 77 K. Namely low temperature fatigue obviously accentuated the subsurface crack initiation. **Figure 8** represents the fracture surfaces of the samples failed by surface crack initiation ((a), (c) and (e)) and subsurface crack initiation ((b), (d) and (f)). At low magnification the crack initiation sites (Stage I crack) in both

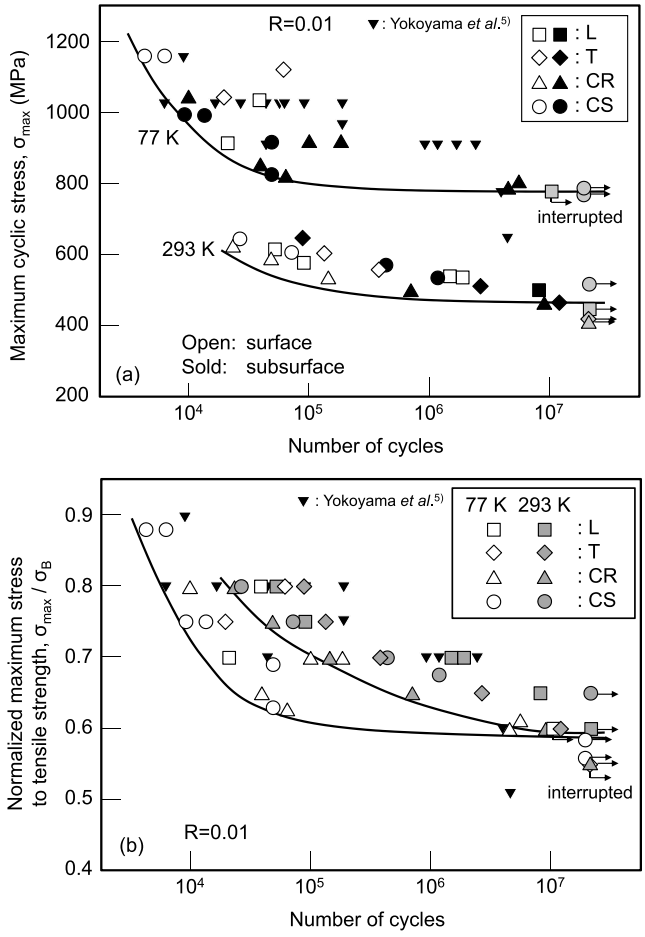

Fig. 7. S–N data of the tested materials at 77 K and 293 K (a) and their stresses normalized by tensile strength (b).

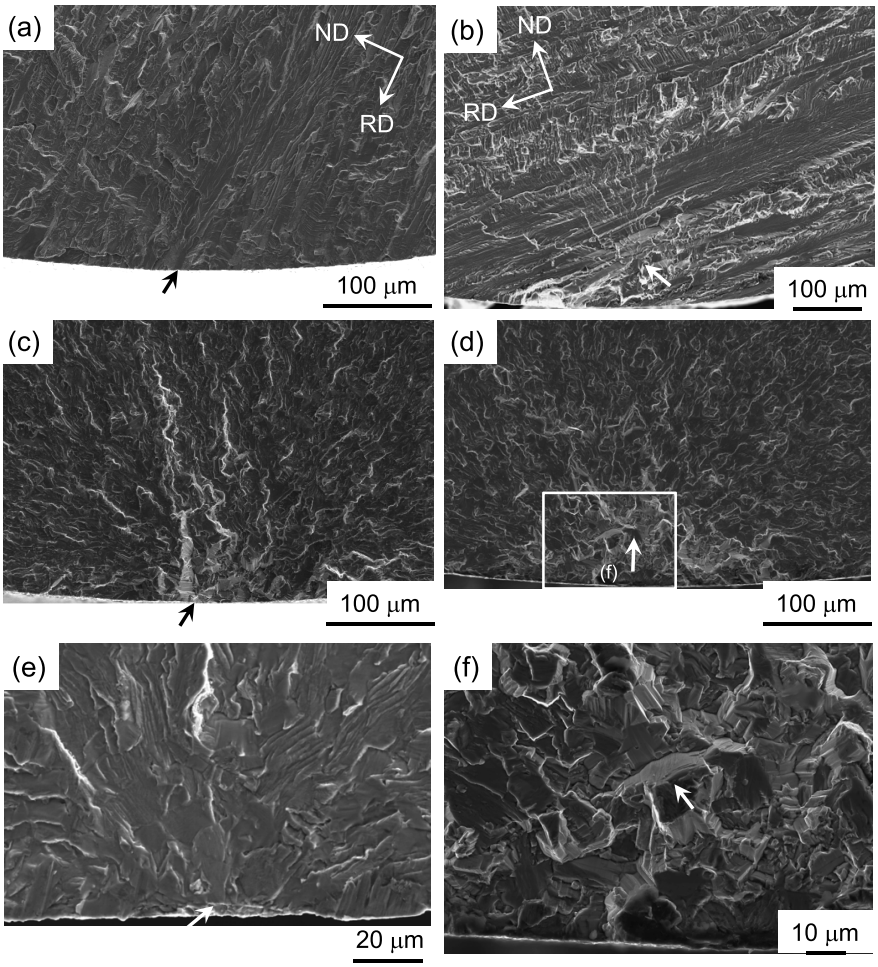

Fig. 8. Crack initiation sites of the test materials: (a) T, 77 K, σ_{max}=1 046 MPa, Nf=19 300 cycles, (b) T, 293 K, σ_{max}=637 MPa, Nf=85 578 cycles, (c) CS, 293 K, σ_{max}=599 MPa, Nf=72 424 cycles, (d) CS, 293 K, σ_{max}=539 MPa, Nf=1 166 619 cycles, (e) CS, 77 K, σ_{max}=1 161 MPa, Nf=6 950 cycles, (f) magnified image of photograph (d). Arrows indicate the initiation sites.

types appear flat and are inclined to the principal stress axis, and fatigue crack growth gives an appearance in a radial pattern from the initiation sites. No defect such as inclusion or pore was detected at the initiation sites. The subsurface crack initiation sites consisted of one or more facets. Facet or facets were also detected at the surface crack initiation sites as shown in Figs. 8(a), 8(c) and 8(e). Each facet can be fitted to an α grain judging from its morphology and size in every material. In the CR, separation was observed along TD on the Stage II or Stage III fracture surface.

The subsurface crack initiation sites in the L, T and CR were inclined about 45 degrees to the principal stress axis analyzed by 3D laser microscopy. The planes of aligned facets in an initiation site as shown in Fig. 8(b) exhibited almost the same inclination macroscopically, which may be resulted from the microtexture (macrozone) with aligned α grains with a similar crystal orientation. In the CS, the subsurface crack initiation sites at 293 K were consisted of facets with almost parallel and perpendicular to the principal stress axis (RD) as shown in Fig. 8(f), where some facets parallel to the principal stress axis are seen as thin lines in the figure (facet plane is near normal to the figure). Then two types of microcracks at least are responsible to generate the subsurface crack initiation sites. Furthermore, coalesced facets with a flat surface at the crack initiation sites in the CS appeared at 77 K as shown in Fig. 8(e), which exhibited nearly perpendicular to the principal stress axis and did not fit to (0001) plane because of its fiber texture. Thus, the non-basal microcracks such as $\{10\bar{1}0\}$}[9] should be taken into account for the subsurface crack generation in the CS as discussed in below, even though the (0001) microcrack and its growth are normally predominant.[1,2]

4. Discussion

4.1. Size of Subsurface Crack Initiation Site

Subsurface microcrack which becomes for a fatal crack is always competitive and depends on the size and the applied stress level. The size of the subsurface crack initiation sites was increased as the decrease of maximum cyclic stress.[2,5,6] In the case of postulating the equivalent crack projected on the propagating plane, the square root of subsurface crack area as defined in above, $\sqrt{area}$, corresponds to its length.[16] Using the crack length parameter $\sqrt{area}$, the size of subsurface crack initiation site can be related to the maximum cyclic stress range, $\Delta\sigma_{max}$, as shown **Fig. 9**(a).

Kitagawa *et al.*[22] and Murakami[16] proposed that the fatigue limit of the material containing pre-existing defects was determined from the relationship between the defect size and threshold stress range. The ideas are based on the

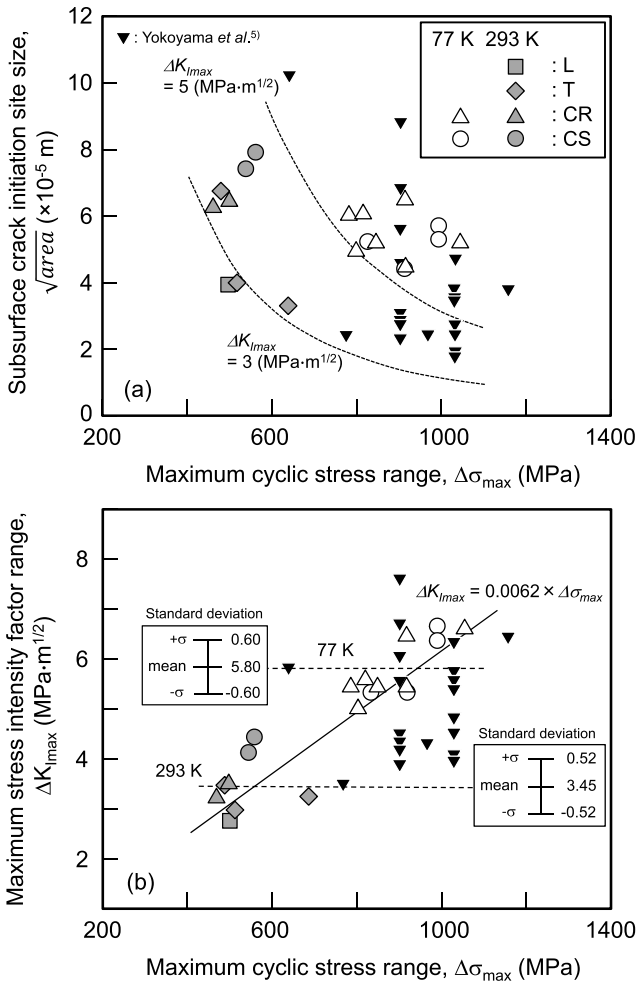

Fig. 9. Relationship between maximum cyclic stress range and subsurface crack initiation site size (a) and estimated maximum stress intensity factor range (b).

assumption that a small defect is equivalent to a microcrack (Stage I crack) and that the microcrack growth is retained under the fatigue limit. Thus, the threshold stress intensity range, ΔK_{th}, determines the fatigue limit stress range for a Stage I crack size. In addition, the simplifications are made as follows; the deformation mode at the crack tip is Mode II in Stage I and the Mode I in Stage II; only principal stress controls the Stage II crack propagation; dependence of microcrack length on ΔK_{th} is neglected. Then a simple approximated equation to give the maximum stress intensity factor range, ΔK_{Imax}, at the crack tip is represented as follows:

$$\Delta K_{Imax} = A \cdot \Delta\sigma_{max}\sqrt{\pi\sqrt{area}} \quad \cdots\cdots\cdots\cdots (1)$$

where A is 0.5 in this study as the coefficient of subsurface crack. The fatigue crack growth modeling that based on linear fracture mechanics under the Mode I condition provided a good estimate of the stress intensity range for subsurface crack growth in Ti–Fe–O alloy.[23] The $\sqrt{area}$ was increased as the decrease of $\Delta\sigma_{max}$ in Fig. 9(a). According to the Eq. (1), the critical size of subsurface crack initiation site is given by the $\Delta\sigma_{max}$ through the concept of ΔK_{th} = constant. Since the microcrack grows until it finally forms the initiation site (facet or facets) over a critical size, the $\sqrt{area}$ data are scattered and higher than a critical length as demonstrated by threshold curves of ΔK_{Imax} = constant in Fig. 9(a). The texture or microtexture in microstructure may assist the spontaneous microcrack growth forming facets aligned and giving longer microcrack length at the higher stress level, as microstructure affected on crack propagation life in the Ti–Fe–O alloy.[23]

Figure 9(b) represents the calculated ΔK_{Imax} for the subsurface crack initiation sites as a function of $\Delta\sigma_{max}$ using $\sqrt{area}$. The ΔK_{Imax} data at 77 K were less scattered than the previous ones,[5] and their mean values were almost equal as approximately 5.8 MPa·m$^{-1/2}$. However, the mean value at 77 K is higher than that at 293 K (3.45 MPa·m$^{-1/2}$) as indicated by their standard deviations in Fig. 9(b). Even though the temperature dependence of critical resolved shear stress (CRSS) in the principal slip systems affects the restriction to $\{10\bar{1}0\}<11\bar{2}0>$ primary slip and planar slip manner at 77 K,[7] following considerations may be available. When the temperature dependence of ΔK_{Imax} value is neglected, given data sequence in Fig. 9(b) is represented as $\Delta K_{Imax} = 0.0062\times\Delta\sigma_{max}$ by least-squares method. The relationship between $\sqrt{area}$ and $\Delta\sigma_{max}$ clearly reveals the dependence of crack length on ΔK_{th}, so that the microcrack growth may be roughly controlled by the critical condition, ΔK_{th} = constant, but the temperature and stress dependences on ΔK_{th} should be taken into account for.

4.2. Transgranular Microcrack and Its Growth

The facet planes at the subsurface crack initiation sites in the L, T and CR specimens failed at 77 K and 293 K were identified as (0001) by EBSD analysis. **Figure 10** represents the matching halves of an initiation site in the CR at 77 K. Facets indicated as 1, 2 and 3 at the initiation sites were inclined approximately 45 degrees to the principal stress axis. Tear ridge between facets and steps on a facet were also appeared. Figures 10(e) and 10(f) are magnified images at microcracking (by arrows) point and its growth on a facet in the matching halves. **Figure 11** shows the tilted image of the site to identify the facet plane by EBSD pattern analysis. An example of the EBSD pattern obtained from the facet 1 is shown in Fig. 11(c). Dark region was caused due to shadowing of the pattern by the adjoining fracture surface. In spite of the fact that part of the EBSD patterns was missing, the indexing yielded an unambiguous and reproducible crystallographic orientation for each facet as shown in Fig. 11(b). Thus, the aligned facets in Fig. 10(c) were (0001) transgranular microcrack, so that the microcrack and its growth were on the (0001) plane of α grains. Morita *et al.*[10] evaluated the plastic deformation relaxing the stress field under the tension or simple shear mode in α-titanium alloy using Taylor model. The localized basal slip on (0001) under the simple shear mode (Mode II and/or Mode III) may assist the growth of (0001) microcrack.

Then the microstructural modification such as grain refinement and random orientation distribution with (0001)// RD texture in the CS may have an advantage for preventing microcrack growth and coalescence under shear stress mode as well as microcracking under opening stress on (0001). Two types of facets at subsurface crack initiation sites were detected in the CS specimens failed at 293 K as mentioned in the section 3.3. The facet formed nearly parallel to the

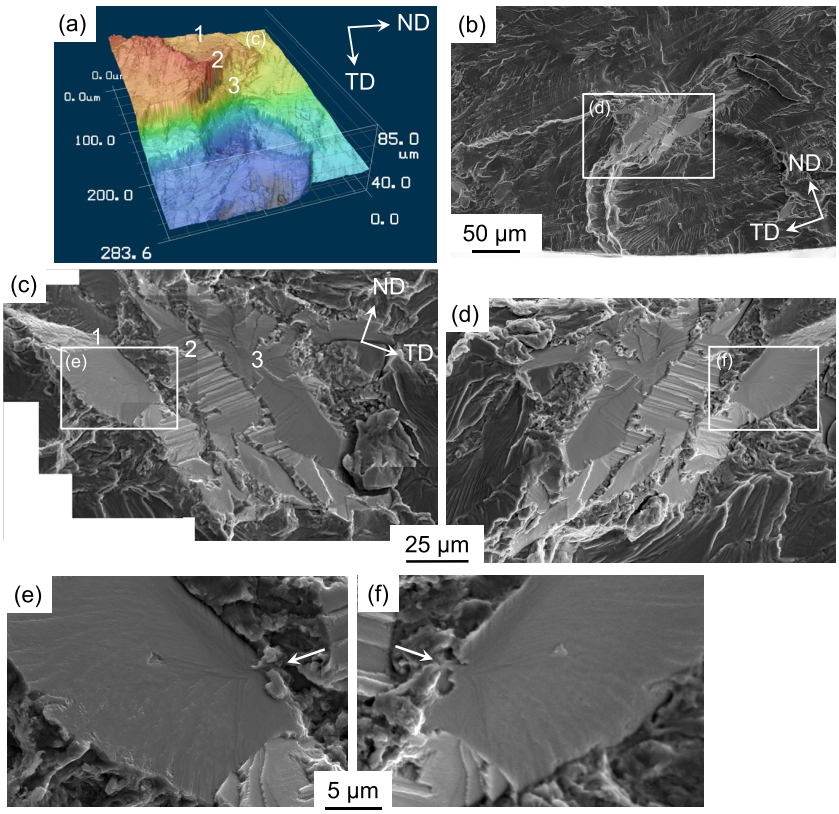

Fig. 10. A subsurface crack initiation site in CR specimen failed at 77 K (σ_{max}=785 MPa after 4 405 468 cycles): (a) 3D view by laser microscopy and (b) whole view of the site in the other side of (a). Photographs (c) and (d) are matching halves of the site. Numbers of 1–3 indicating facets are corresponded in (a) and (c). Photographs (e) and (f) are magnified images at microcracking (by arrows) in photographs (c) and (d). (Online version in color.)

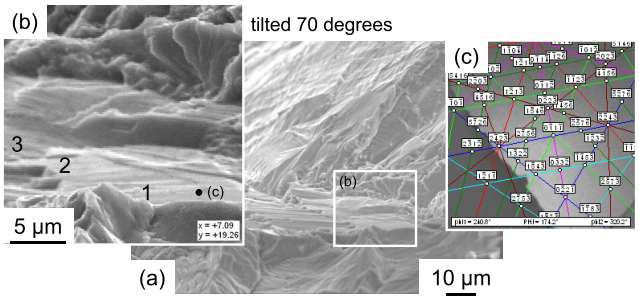

Fig. 11. Tilted image shown in Fig. 10(c) with 70 degrees (a), its magnified image of the site (b) and an example of indexing overlaid on EBSD pattern (c) from facet 1. Numbers of 1–3 indicate the facets shown in Fig. 10(c). (Online version in color.)

principal stress axis at the site was also identified as (0001) plane. The (0001) facets reflected on the texture of the CS were coalesced through the other type of facet with perpendicular to the principal stress axis in order to generate the subsurface crack initiation site. In fact the microstructural modification to prevent the growth and coalesce of (0001) facets successfully resulted in the increase of high-cycle fatigue strength at 293 K compared to the L, T and CR materials.

However, no improvement of high-cycle fatigue strength in the CS was achieved at 77 K by comparing with the other materials. **Figure 12** represents matching halves images of a subsurface crack initiation site in the CS failed at 77 K. The facets with a flat surface at the crack initiation site were identified as $\{10\bar{1}0\}$ plane. As an example, the EBSD pattern in Fig. 12(e) obtained from the tilted facet shown in Fig. 12(d) reveals $(01\bar{1}0)$. Figure 12(c) shows the tilted image near the specimen surface beside $\{10\bar{1}0\}$ facet in the other side. Just beneath the specimen surface, (0001) facet was also detected and connected to $\{10\bar{1}0\}$ facet as the illustration in the cross section. Then the (0001) facet may give a trigger to generate the subsurface crack initiation site with $\{10\bar{1}0\}$ facets.

After cyclic deformation at 293 K and 77 K, sub-boundary structures were rearranged in the recovered α grain region of the CR, and dislocation arrays were developed in α grains of the CS.[24] Dislocation movements were restricted to their slip planes of $\{10\bar{1}0\}<11\bar{2}0>$. The temperature dependence of critical resolved shear stress (CRSS) in the principal slip systems strongly affected the restriction to $\{10\bar{1}0\}<11\bar{2}0>$ primary slip and planar slip manner at 77 K.[7] Based on the deformation manner, the models forming $\{10\bar{1}0\}$ facet or facets was proposed as illustrated a schematic diagram in **Fig. 13**. Since deformation constraints in the α grains on the specimen surface are rather flexible than the internal, strain incompatibility may be introduced near the specimen surface. Here we discuss the models divided into three types of crack initiation such as surface crack and subsurface crack at 77 K and 293 K as follows.

4.2.1. Surface Crack Initiation at Higher Stress Level (Fig. 13(a))

Planar slip bands developed on the specimen in cyclically deformed the CS may act as leading to fatigue crack initiation just like persistent slip bands (PSBs).[25] The principal

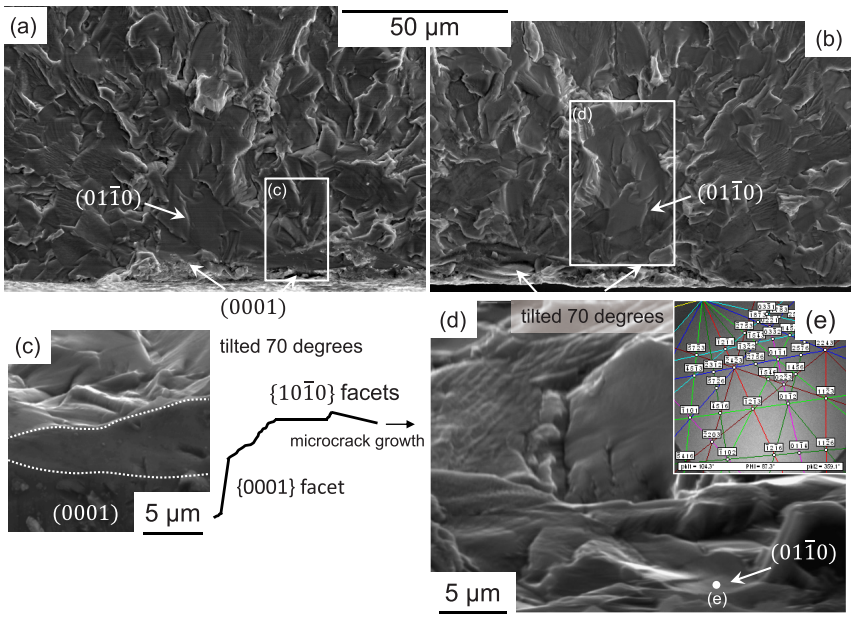

Fig. 12. A subsurface crack initiation site in CS specimen failed at 77 K (σ_{max}=829 MPa after 47 487 cycles). Photographs (a) and (b) are matching halves of near the site. Photograph (c) is 70 degrees tilted and magnified image in photograph (a), and its illustration in the cross section. Photograph (d) is 70 degrees tilted and magnified image in photograph (b), and an example of indexing overlaid on EBSD pattern (e) from (01$\bar{1}$0) facet is built in the photograph (d). (Online version in color.)

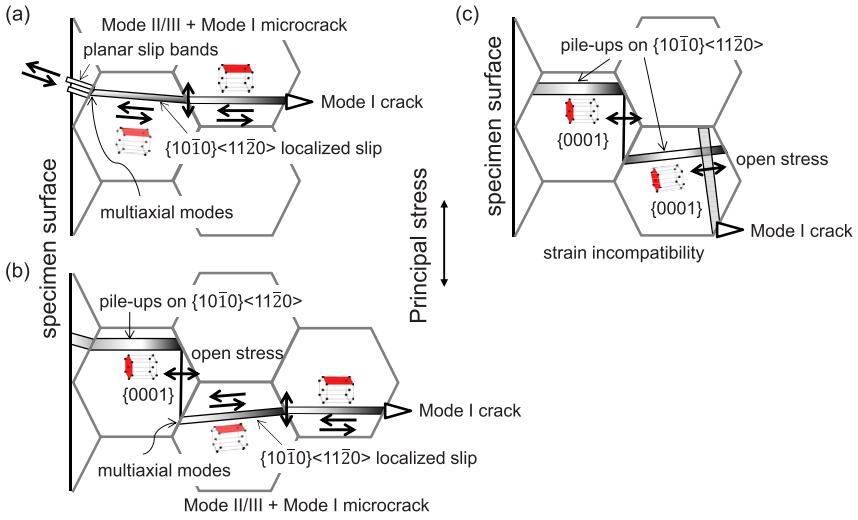

Fig. 13. Schematic illustration of a fatigue crack initiation model proposed in the CS: (a) surface crack initiation, (b) subsurface crack initiation at 77 K and (c) subsurface crack initiation at 293 K. (Online version in color.)

stress applied is almost normal to {10$\bar{1}$0} plane in a number of grains in the CS. Since a stress concentration and a field with multiaxial modes induced by the blocked slip band are locally developed at the grain boundary, the combination of shear stress and opening stress on {10$\bar{1}$0} may act a mode II or III microcracking if the slip system is poorly aligned with <a> prismatic, pyramidal or basal slip systems in the neighboring grain.[26] The microcrack can grow on {10$\bar{1}$0} under superimposed opening (mode I) stress due to the principal stress. When the {10$\bar{1}$0} plane in a neighboring grain is also oriented near normal to the RD, the microcrack can easily grow into the neighboring grain.

4.2.2. Subsurface Crack Initiation at 77 K (Fig. 13(b))

In an α-grain near the specimen surface, {10$\bar{1}$0}<11$\bar{2}$0> primary slip is predominantly operated. As a result, the screw dislocations pile-ups introduce a stress concentration along c-axis, which gives an opening stress on (0001) in the grain. The strain incompatibility in the grain has a potential to cause the shear stress on (0001), which assists the microcrack generation by (0001) slip-off. The (0001) mirocrack provides a stress field with multiaxial modes in the neighboring grain so that the combination of shear stress and opening stress on {10$\bar{1}$0} may also lead to a mode II or III microcracking. The localized shear stress as well as opening (mode I) stress due to the principal stress should be responsible for the microcrack growth on prismatic plane in the neighboring grain. Then the {10$\bar{1}$0} facets growth may appear at 77 K. As in the case of (a) in above, the microcrack can easily grow into the neighboring grain.

4.2.3. Subsurface Crack Initiation at 293 K (Fig. 13(c))

The restriction to $\{10\bar{1}0\}<11\bar{2}0>$ primary slip and planar slip manner at 77 K are rather severe than at 293 K. In addition, the principal stress itself is higher at 77 K than at 293 K. The (0001) mirocrack at 293 K should provide a stress field with multiaxial modes in the neighboring grain, too. Although less opening stress on $\{10\bar{1}0\}$ is poor to generate a mode II or III microcracking, it is considered that the microcrack healing through the dislocation emission at a crack tip promotes the (0001) microcrack in neighbor, and that the (0001) facets are coalesced by bridging $\{10\bar{1}0\}$ facet or intergranular one.

Therefore, the microtexture of (0001) or $\{10\bar{1}0\}$ plane may assist the spontaneous microcrack growth forming facets aligned and giving longer microcrack length. The microstructural modification to refine the α-grain structure and to distribute its crystal orientation randomly is a good solution to improve the high-cycle fatigue strength of titanium alloys such as thermomechanical treated Ti-6Al-4V alloys.[4] However, the resistance of microtexture against microcrack growth should be taken into account.

5. Conclusions

High-cycle fatigue properties of a Ti–Fe–O alloy with different processed products such as rolled plate (L and T), cross-rolled plate (CR) and groove-rolled bar (CS) were evaluated at 77 K and 293 K, and transgranular facets at the crack initiation sites were analyzed to discuss subsurface crack initiation. Major conclusions were summarized as follows.

(1) The rolled plates consisted of recrystallized α grains and recovered α grains. Each α grain was elongated and a macrozone (microtexture) in the recovered α grain region was developed. Fine equiaxed α grains randomly oriented with [0001] perpendicular to tensile axis were produced in the CS.

(2) No significant difference of 10^7 cycles fatigue strength was recognized among the test materials at each temperature, although the CS exhibited an improved fatigue strength in long-life regime at 293 K.

(3) The subsurface crack initiation was dominant in lower stress level and at 77 K. The subsurface crack initiation sites consisted of facet or facets, and each facet was fitted to α grain. The facets were identified as (0001) in the L, T and CR. In the CS, the (0001) facet provided an origin of subsurface crack initiation site, but the $\{10\bar{1}0\}$ facets mainly covered the sites at 77 K.

(4) Using a crack length parameter $\sqrt{area}$, the dependence of subsurface crack initiation site size on the maximum stress range was evaluated. The maximum stress intensity factor range, ΔK_{Imax}, revealed the temperature and stress dependences.

(5) The accumulated open stress along [0001] may be responsible for forming (0001) facets. The (0001) mirocrack may provide a stress field with multiaxial modes in the neighboring grain as well as induced by the blocked slip band. In the CS, the combination of shear stress and opening stress on $\{10\bar{1}0\}$ may lead to a mode II or III microcracking and be responsible for the microcrack growth on prismatic plane in the neighboring grain.

Acknowledgement

The authors wish to thank Drs. Y. Ono, T. Yuri and T. Ogata of National Institute for Materials Science, and Mr. Y. Shindo (now Toyota Industries Corp.) and Dr. N. Koga of Yokohama National University for their help on the experiments.

REFERENCES

1) W. Li and O. Umezawa: *Key Eng. Mater.*, **741** (2017), 76.
2) O. Umezawa and K. Nagai: *ISIJ Int.*, **37** (1997), 1170.
3) H. Yokoyama, O. Umezawa, K. Nagai, T. Suzuki and K. Kokubo: *Metall. Mater. Trans. A*, **31A** (2000), 2793.
4) K. Nagai, T. Yuri, T. Ogata, O. Umezawa, K. Ishikawa, T. Nishimura, T. Mizoguchi and Y. Ito: *ISIJ Int.*, **31** (1991), 882.
5) H. Yokoyama, O. Umezawa, K. Nagai and T. Suzuki: *ISIJ Int.*, **37** (1997), 1237.
6) O. Umezawa, K. Nagai and K. Ishikawa: *Tetsu-to-Hagané*, **76** (1990), 924.
7) M. Morita and O. Umezawa: *Mater. Trans.*, **52** (2011), 1595.
8) I. Bantounas, D. Dye and T. C. Lindley: *Acta Mater.*, **57** (2009), 3584.
9) E. E. Sackett, L. Germain and M. R. Bache: *Int. J. Fatigue*, **29** (2007), 2015.
10) M. Morita and O. Umezawa: Proc. 12th World Conf. on Titanium, Vol. 2, ed. by L. Zhou, *et al.*, Science Press Beijing, Beijing, (2012), 1100.
11) M. R. Bache: *Int. J. Fatigue*, **25** (2003), 1079.
12) M. S. Paterson: *J. Appl. Phys.*, **23** (1952), 805.
13) H. J. Bunge: Texture Analysis in Material Science, Butterworths, London, (1982), 4.
14) M. Dahms and H. J. Bunge: *J. Appl. Crystallogr.*, **22** (1989), 439.
15) M. Hamada and O. Umezawa: *ISIJ Int.*, **49** (2009), 124.
16) Y. Murakami: *Tetsu-to-Hagané*, **75** (1989), 1267.
17) P. A. Davies and V. Randle: *J. Microsc.*, **204** (2001), Part 1, 29.
18) V. Shinha, M. J. Mills and J. C. Williams: *Metall. Mater. Trans. A*, **37A** (2006), 2015.
19) H. Inoue: *Kinzoku*, **69** (1999), 30.
20) W. Li, O. Umezawa and N. Koga: *ISIJ Int.*, **58** (2018), 359.
21) H. Inoue and N. Inakazu: Proc. Int. Conf. on Recrystallization in Metallic Materials (Recrystallization'90), ed. by T. Chandra, TMS, Warrendale, PA, (1990), 687.
22) H. Kitagawa, S. Takahashi, C. M. Suh and S. Miyashita: Fatigue Mechanisms, ASTM STP 675, ASTM, Philadelphia, PA, (1978), 420.
23) O. Umezawa, M. Hamada and T. Tatsumi: *Procedia Mater. Sci.*, **12** (2016), 48.
24) W. Li and O. Umezawa: Proc. 13th World Conf. on Titanium, ed. by V. Venkatesh, *et al.*, TMS, Warrendale, PA, (2016), 843.
25) J. Man, K. Obrtlík and J. Polák: *Philos. Mag.*, **89** (2009), 1295.
26) Y. Guo, T. B. Britton and A. J. Wilkinson: *Acta Mater.*, **76** (2014), 1.